Faraday Discussions
Cite this: *Faraday Discuss.*, 2026, **264**, 231

PAPER

Reactivity of high-entropy alloy nanoparticles under O_2 studied by *in situ* transmission electron microscopy†

Syrine Krouna, Nathaly Ortiz Peña, Christian Ricolleau, Guillaume Wang, Adrien Moncomble, Damien Alloyeau* and Jaysen Nelayah*

Received 26th May 2025, Accepted 25th June 2025
DOI: 10.1039/d5fd00090d

The gas reactivity of high-entropy nanoalloys (HENAs) is an emerging area of research with significant potential for applications in catalysis, gas sensing, hydrogen storage, and corrosion resistance. Insights into the structure–reactivity relationships that dictate the behavior of HENAs in reactive gas environments are critical for optimizing their performance across these applications. However, understanding the complex structural attributes of HENAs, such as size, shape and structure in response to a gas stimulus, remains challenging because of the limited accessibility to methods capable of probing these attributes under *in situ* or *operando* conditions. Here, we performed aberration-corrected environmental gas scanning transmission electron microscopy (STEM) observations to investigate the atomic and chemical structures of quinary CoNiCuPtAu HENAs in response to pure oxygen exposure at atmospheric pressure and elevated temperatures. The nanoparticles were fabricated by pulsed laser deposition with a high degree of control over both size and composition. Atomic-scale STEM imaging combined with energy dispersive X-ray (EDX) spectroscopy at the single particle level revealed a complex structural and chemical evolution pathway for CoNiCuPtAu HENAs under oxygen at atmospheric pressure during progressive heating up to 700 °C. Notably, we have identified substantial mass transfers between nanoparticles accompanied by oxygen-induced demixing of components, nanovoid formation and the stabilization of platelet-like nanostructures crystallizing as a Co–Ni oxide solid solution.

1. Introduction

Since the seminal work by Yao *et al.*,[1] mixing multiple metals at the nanoscale to form so-called high-entropy nanoalloys (HENAs) has emerged as a novel strategy for expanding the diversity of metallic nanoparticles (NPs). The combination of

Université Paris Cité, CNRS, Laboratoire Matériaux et Phénomènes Quantiques, 75013 Paris, France. E-mail: damien.alloyeau@u-paris.fr; jaysen.nelayah@u-paris.fr

† Electronic supplementary information (ESI) available. See DOI: https://doi.org/10.1039/d5fd00090d

atoms with different physicochemical properties, such as atomic radii, cohesive energy, and potential energy, results in a rich variety of atomic and chemical structures. These are typically characterized by a high density of structural defects and significant lattice distortion.[2–5] Consequently, HENAs are proposed to exhibit unusual or enhanced gas reactivity compared to conventional alloys.[6,7] The gas reactivity of HENAs is an emerging field with promising applications in catalysis,[8–10] gas sensing,[11] hydrogen storage[12] and corrosion resistance.[13,14] To advance both fundamental understanding and technological applications, there is, however, an urgent need for *in situ* and *operando* techniques that can unravel the structure–reactivity relationships governing HENAs' behavior under reactive gas environments. However, studies focusing specifically on the gas-phase interactions of HENAs using these advanced techniques remain limited.[15–17] For example, environmental gas transmission electron microscopy (TEM) has been employed to study both the oxidation of FeCoNiCuPt HENAs in dry air[15] and their reduction under atmospheric hydrogen.[16] These investigations have revealed the complex and dynamic nature of HENAs under gas environments and called for further studies that are capable of probing the structural dynamics of HENAs under relevant gas atmospheres and temperatures, while simultaneously capturing their specific reactivity. Such insights are essential for elucidating how the atomic and chemical structures of HENAs influence their reactivity and how these complex structures, in turn, evolve under realistic reaction conditions. In this context, the present study investigates the reactivity and structural dynamics of CoNiCuPtAu HENAs towards oxygen at atmospheric pressure and high temperatures, using aberration-corrected environmental gas TEM. This approach allows us to capture the structural and chemical dynamics of the nanoalloys under oxidative conditions in real-time and down to the atomic scale, providing new insights into how the stability of HENAs is influenced by reaction conditions.

2. Experimental section

2.1 Synthesis of HENAs by pulsed laser deposition

Pulsed laser deposition (PLD) has been widely used for the synthesis of bimetallic nanoalloys.[18] This fabrication method is based on the ablation of ultra-pure monometallic targets in a high-vacuum chamber using laser irradiation, here a COMPex KrF excimer laser. Alternate ablation of pure metal targets enables the formation of nanoalloys with controlled size and composition on a chosen substrate. The experimental conditions for the fabrication of sub-10 nm CoNiCuPtAu NPs with near equiatomic composition were reported by Barbero *et al.*[19] In the present study, the same HENA system was studied with the nanoparticles deposited on the SiN membrane of a heating MEMS chip, commercialized by Protochips for *in situ* TEM investigations. During deposition, the substrate temperature was set as 600 °C, with a laser frequency of 5 Hz and a total nominal thickness of 4 nm. The deposition rate of each metal was measured prior to synthesis using a quartz crystal microbalance.

2.2 *In situ* scanning transmission electron microscopy

In situ transmission electron microscopy experiments were carried out on a double aberration-corrected JEOL ARM 200F microscope equipped with a cold

field emission gun operating at 200 kV.[20] A Protochips Atmosphere™ high-pressure gas cell (HPGC) was used for *in situ* STEM observations under 1 atm O_2 gas pressure. The HPGC comprises two silicon microchips (E-chips) aligned face-to-face in a closed-cell configuration. The smaller E-chip (2 mm × 2 mm × 300 μm) features a 50-nm-thick amorphous SiN window, whereas the larger E-chip (6 mm × 4.5 mm × 300 μm) carries a SiC membrane patterned with six electron-transparent windows (30-nm-thick SiN) for imaging. The CoNiCuPtAu HENAs were synthesized directly on the large E-chip. After assembly of the gas cell, the latter was purged with pure argon (from MESSER; purity ≥ 99.9999%) gas before introducing ultrapure oxygen (from MESSER; purity ≥ 99.9995%) under continuous flow conditions. The sample was heated *via* resistive heating of the SiC membrane, with a closed-loop temperature control system ensured accurate temperature regulation. *In situ* imaging and video recording were captured in STEM mode using both high-angle annular dark-field (HAADF) and bright-field (BF) detectors, with a 20.5 mrad convergence semi-angle for BF-STEM imaging and between 68 and 280 mrad for HAADF-STEM imaging. Short pixel dwell times (2–3 μs) were used to minimize beam-induced damage. The electron beam was blanked between data capture sessions to further limit electron dose.

3. Results

Using high-resolution BF-STEM and HAADF-STEM imaging combined with spatially-resolved energy dispersive X-ray spectroscopy (EDS), we first investigated the size, structure, and compositional evolution of CoNiCuPtAu NPs under 1 atm oxygen atmosphere during progressive heating up to 700 °C (see ESI Fig. S1† for the heating profile). Pure oxygen was introduced at 200 °C, which was the starting

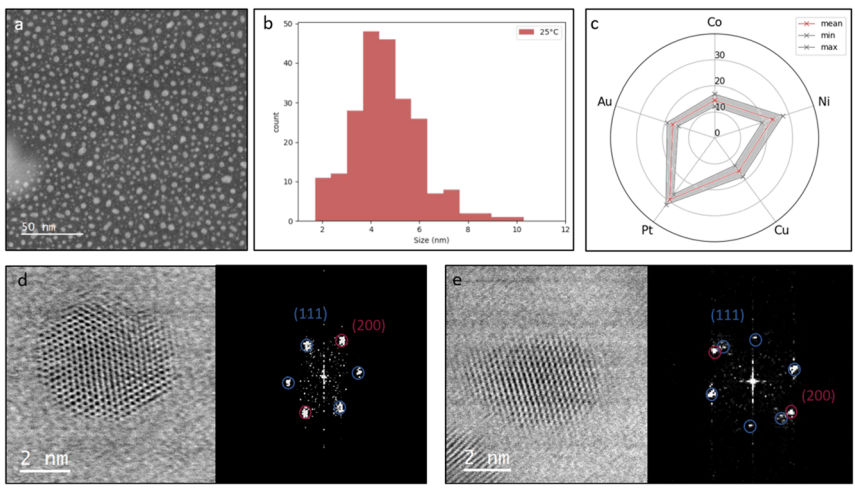

Fig. 1 As-prepared CoNiCuPtAu HENAs. (a)–(e) HENA fabricated on the amorphous SiN membrane of a Protochips HPGC. (a) HAADF-STEM image of the high entropy alloy (HEA) NPs. (b) Particle size distribution of NPs with a mean diameter around 4 nm. (c) Mean composition of NPs represented by the red line and with the shaded grey area indicating the standard deviation. BF-STEM images of a (d) FCC monocrystalline NP observed along its [110] zone axis and (e) an FCC twinned NP.

temperature for the present studies, knowing that less electron-beam-induced contamination occurs at this temperature compared to room temperature. The choice of the temperature range is justified by our previous study on the thermal behaviour of quinary CoNiCuPtAu HENAs in vacuum.[21] In the present study, the same temperature range is applied to enable a direct and meaningful comparison of their thermal stability in vacuum and in an O_2 atmosphere. As shown in Fig. 1b, the as-synthesized NPs under Ar, before oxygen exposure, exhibit a size distribution ranging from 2 to 10 nm, with an average diameter of 4.6 ± 1.4 nm. STEM-EDS analysis of single NPs revealed a mean composition of $Co_{15}Ni_{23}Cu_{16}Pt_{29}Au_{17}$ with a standard deviation of 3% (Fig. 1c). As shown already,[19,21] high-resolution

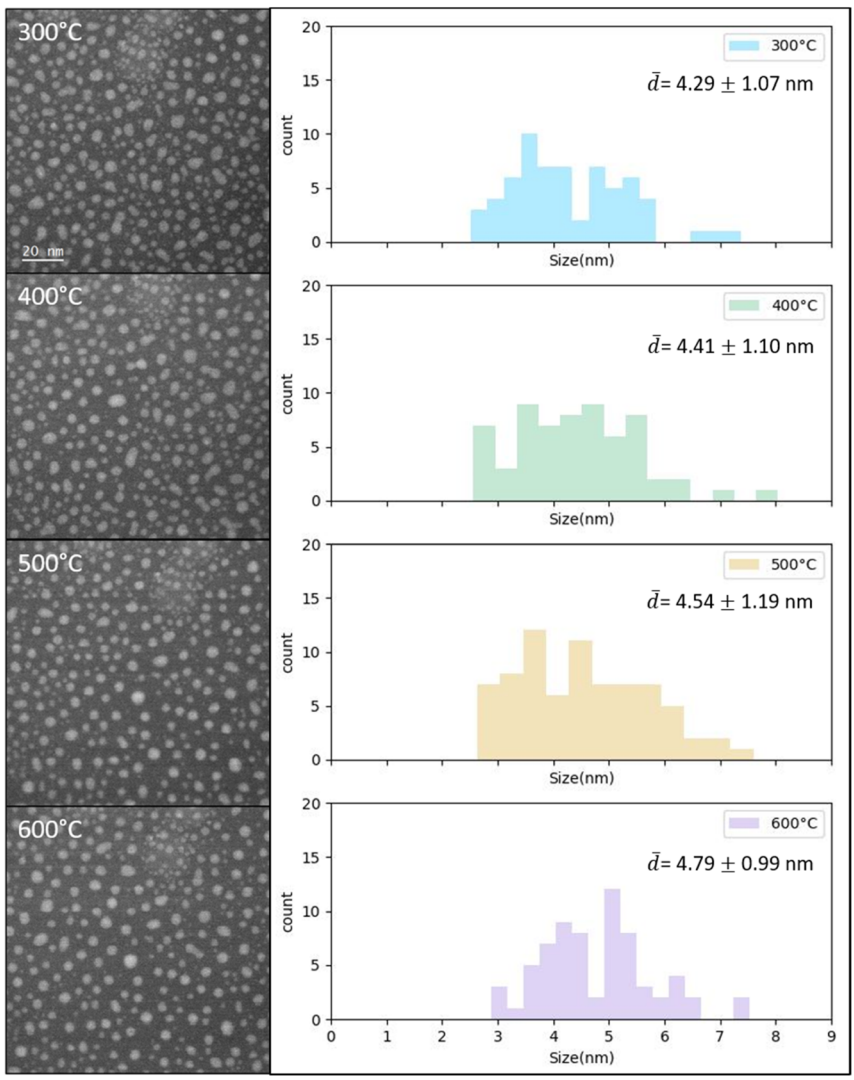

Fig. 2 Low-resolution STEM image series showing the evolution of a HENA under O_2 as a function of the temperature with the corresponding size distribution of the NPs. The corresponding mean diameter $\bar{d}$ is indicated in the top-right corner.

STEM imaging here confirmed that CoNiCuPtAu HENAs crystallize in a face-centered cubic (FCC) solid solution, leading either to FCC single nanocrystals (Fig. 1d) or twinned FCC structures (Fig. 1e; see also ESI, Fig. S2†). As discussed in previous work,[19,21] CoNiCuPtAu HENAs synthesized *via* PLD form small monocrystalline NPs, under 3 nm, while twinned structures are only observed in bigger NPs.

Fig. 2 presents a temperature series of HAADF-STEM images of the $Co_{15}Ni_{23}Cu_{16}Pt_{29}Au_{17}$ NPs under O_2 between 300 and 700 °C. The corresponding NP size distributions, deduced from the analysis of 70 NPs, are represented alongside. We observe that as the temperature increases under oxygen, the particle size distribution remains unimodal with the mean NP diameter showing minimal variation throughout the heating cycle. Based solely on this size analysis, it would be tempting to suggest that the CoNiCuPtAu HENAs remains structurally and chemically stable under the applied conditions.

However, high-resolution STEM analysis (Fig. 3), particularly *in situ* STEM video recordings to track particle stability and mobility on the SiN substrate during heating under O_2 (ESI Video S1†), reveals the activation of the well-known particle growth mechanisms under thermal stimulus: coalescence and Ostwald ripening.[18,22,23] Such growth processes are accompanied by substantial interparticle mass transfer that leads to an increase in the mean particle size.

Yet, this observation is in contradiction to the relatively stable particle size distribution revealed by particle size analyses. This apparent contradiction can be explained by an oxygen-induced phenomenon that triggers the demixing of components at high temperatures, followed by phase segregation and subsequent structural rearrangement. In particular, STEM imaging revealed the formation of platelet-like structures that, as they grow, draw mass from the NPs and offset the expected size increase due to coalescence and Ostwald ripening. The platelets are extremely thin and, consequently, exhibit lower *Z*-contrast than the NPs, which accounts for their visibility only in high-resolution STEM images (Fig. 4a and b). To identify these structures, we combined high-resolution BF-STEM imaging and compositional analysis *via* STEM-EDS. Atomic-scale analysis of the BF-STEM images revealed two distinct *d*-spacings of 0.215 nm and 0.241 nm, measured within the platelets. In addition, as shown in Fig. 4d, STEM-EDS confirmed that

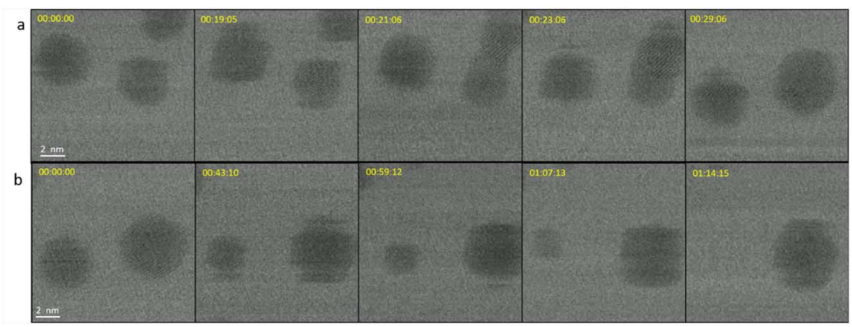

Fig. 3 Coarsening events recorded at 700 °C involving (a) coalescence and (b) Ostwald ripening. The acquisition time is indicated in the top-left corner of each image (see associated ESI Video S1†).

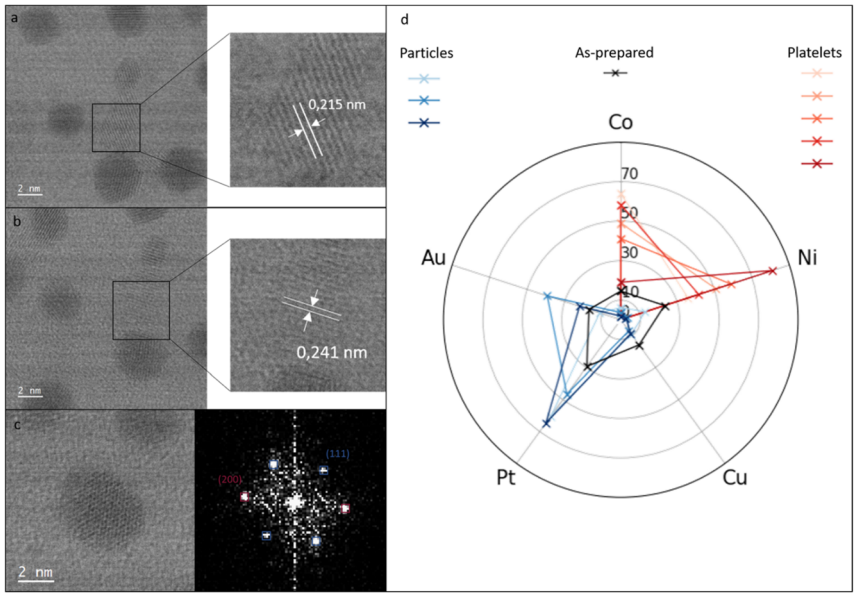

Fig. 4 (a), (b) and (c) High-resolution BF-STEM images under O_2 at 200 °C after heating up to 700 °C presenting structural evolution of CoNiCuPtAu NPs and formation of $Ni_{1-x}Co_xO$ platelets. (a) and (b) High-resolution BF-STEM images showing platelets with the corresponding *d*-spacing. (c) High-resolution BF-STEM image of a AuPtCu NP observed along the [110] zone axis. (d) Spider plot showing the composition of the platelets (red lines), the particles (blue lines) and, for reference, the as-prepared composition (black line).

these structures contain exclusively cobalt (Co) and nickel (Ni). By comparing our structural and compositional findings with literature data,[24] we identify the platelets as a Co–Ni oxide solid solution, $Ni_{1-x}Co_xO$. This compound adopts a NaCl-type crystal structure, where O^{2-} ions occupy the octahedral interstitial sites and Co^{2+}/Ni^{2+} cations randomly populate the FCC lattice positions (see the structural model in the ESI, Fig. S3†).

Simultaneously, as shown in Fig. 4c, the remaining rounded NPs are well-alloyed, retaining their FCC structure. The compositional spider plot (Fig. 4d)

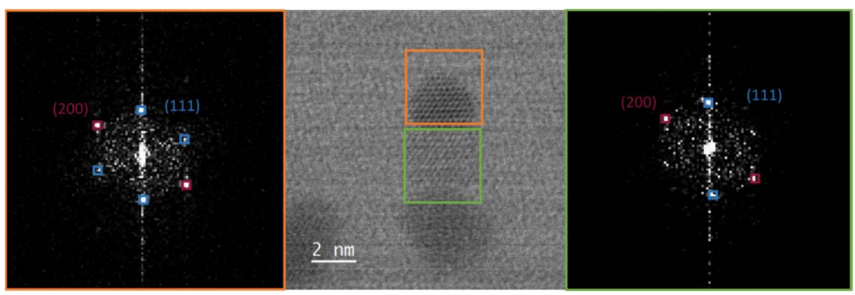

Fig. 5 In the middle, high-resolution STEM image illustrating the epitaxial growth of the $Ni_{1-x}Co_xO$ platelets on the NPs. The FFT images to the left and right of the HR-STEM image are calculated on the NP (orange frame) and on the platelet (green frame), respectively.

highlights the complementarity of the elemental distributions between the platelets and the rounded NPs. These latter are thus mainly composed of Au, Pt and Cu.

Interestingly, high-resolution structural analysis further reveals that the $Ni_{1-x}Co_xO$ platelets grow epitaxially on the rounded NPs. As illustrated in Fig. 5 and ESI Fig. S4,† the platelets commonly share crystallographic orientations with the rounded NPs, primarily along the (111) and (200) planes.

Furthermore, the presence of oxygen triggers the formation of voids within many NPs, as observed by comparing Fig. 6a and b (supplementary high-

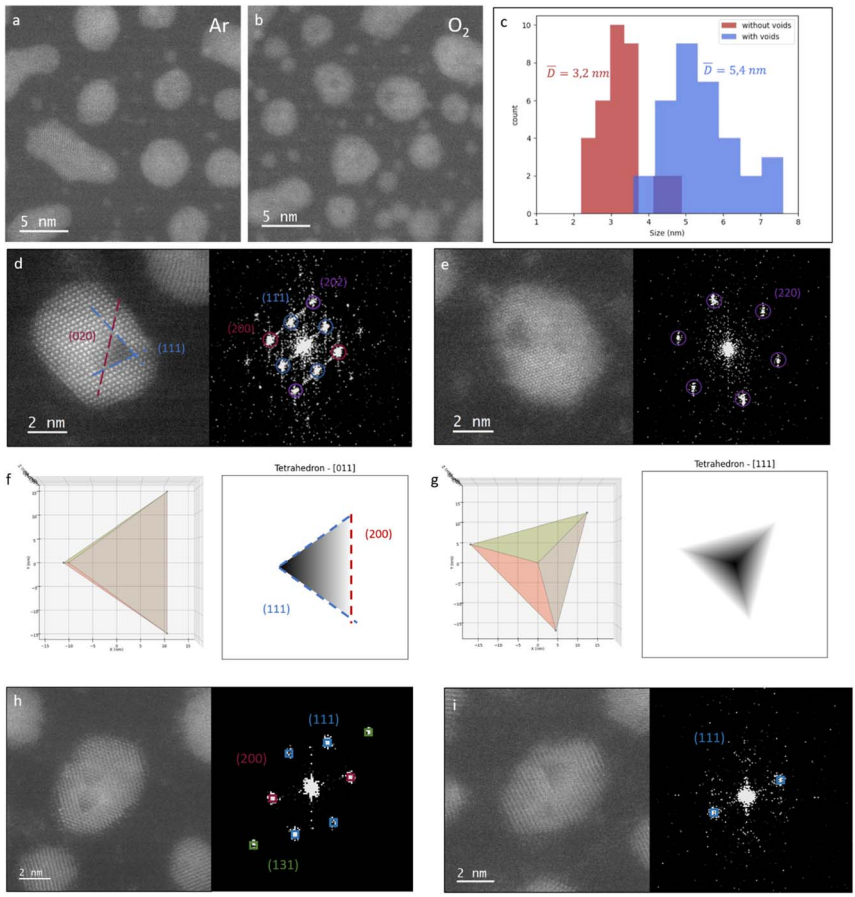

Fig. 6 HAADF-STEM images showing the voids formed in the NPs when the NPs are exposed to oxygen at 200 °C. (a) NPs under Ar before O_2 exposure and (b) under O_2. (c) Size distribution of NPs with and without voids. (d) and (e) High-resolution HAADF-STEM images of NPs presenting a triangular-shaped void along the [110] and [111] zone axes, respectively. (f) and (g) Tetrahedral 3D models bounded by {111} facets observed along the [110] and [111] zone axes, respectively. The contrast-inverted STEM image of the tetrahedral 3D model calculated by kinematic STEM simulation; the two zone axes are shown alongside. The STEM intensity is inversely proportional to the local thickness upon contrast reversal. (h) and (i) High-resolution HAADF-STEM images of NPs containing multiple triangular-shaped voids. For stability and in order to keep the spatial resolution, high-resolution images were acquired under vacuum at room temperature.

resolution HAADF-STEM images are presented in ESI Fig. S5†). This phenomenon is attributed to the Kirkendall effect, which arises from the difference in diffusion rates between outward-migrating metal atoms and inward-diffusing oxygen. Notably, this effect, which is well-documented in bulk metallic systems,[25,26] as well as monometallic[27–29] and bimetallic NPs,[30–35] has not previously been reported in HENAs. These voids are observed exclusively in larger NPs; as shown in Fig. 6c, NPs smaller than 4 nm do not exhibit any internal cavities (see ESI Video S2†). Additionally, very large NPs exhibit multiple voids as illustrated in Fig. 6h and i. Once formed, the voids are highly stable. As shown in the ESI, Videos S3 and S4,† they appear unchanged even when the NPs undergo coalescence. When the NPs are observed along the [110] zone axis, the projected shape of the voids is triangular, characterized by a sharp apex formed between the two edges perpendicular to the [111] directions, and a diffuse edge which is perpendicular to [100] (Fig. 6d). When the NPs are observed along the [111] zone axis, the projected shape of the voids presents a triangular-like shape with a dark barycenter (Fig. 6e). To identify the three-dimensional geometry of these voids, their characteristic STEM contrasts along the [110] and [111] zone axes were compared with the STEM contrast for a tetrahedral solid volume bounded by {111} facets in vacuum simulated using kinematic STEM approximations (for more information, see the supporting "Voids simulation" section and Fig. S6 in the ESI†).[36] By inverting the STEM contrast in the simulations, the resulting HAADF images of the solid tetrahedral model are qualitatively similar to those of a tetrahedral void in a bulk material viewed along various zone axes (Fig. 6f and g). Upon contrast reversal, the simulated STEM contrast closely matches those of the experimentally observed void shapes, providing strong evidence for the tetrahedral 3D shape of the voids.

4. Discussion

The structural behavior of CoNiCuPtAu HENAs in an oxygen environment is largely governed by the differing reactivities of the constituent elements towards oxygen. Notably, the structural and chemical transformations revealed in the present work differ significantly from those observed when the same high entropy alloy (HEA) NPs undergo thermal treatment in vacuum. In a previous work, where we studied the evolution of the atomic structure of CoNiCuPtAu HENAs between 25 and 700 °C using *in situ* thermal TEM and molecular dynamics simulations,[21] we highlighted a chemical evolution characterized by the progressive surface segregation and subsequent evaporation of gold and copper atoms from the NPs. This selective elemental segregation was shown to be reinforced by severe shape and surface restructuring upon particle coalescence that occurs at high temperatures (above 400 °C). In particular, experimental observation and numerical simulations revealed that thermally driven atomic diffusion under vacuum is surprisingly very active in CoNiCuPtAu quinary nanoalloys. In particular, we demonstrated that under vacuum conditions, the structural evolution of CoNiCuPtAu HENAs was governed purely by thermodynamic factors. Surprisingly, their atomic and chemical structures are primarily dictated by surface effects rather than their mixing entropy. The selective segregation of Au and Cu is attributed to their lower surface energies compared to the other constituent elements.

In contrast, the presence of oxygen significantly alters this behavior with the oxidation kinetics prevailing over thermodynamic factors and actively directing the structural evolution. As reported by Song *et al.*,[15] based on the formation energy, the tendency for metal oxide formation decreases in the following order for the three non-noble metals considered in this work: Co (1.3 eV per atom), Cu (1.0 eV per atom) and Ni (0.9 eV per atom). This hierarchy explains the preferential oxidation of Co and Ni when CoNiCuPtAu HENAs are exposed to oxygen at atmospheric pressure. Interestingly, copper oxides are absent among the oxidation products. This can be attributed to two principal factors: the relatively low diffusion coefficient of copper compared to the ones for cobalt and nickel,[15] and the stabilizing effect of gold on copper within the NPs, which likely not only hinders the migration of copper to the surface but also enhances its oxidation resistance. Indeed, it has been already shown[37,38] that the presence of gold enhances the oxidation resistance of copper, particularly in nano-sized objects. It has been proposed that gold reduces the oxidation potential of copper by altering the local electronic structure at the NP surface, decreasing the ability for oxygen to interact with and oxidize copper.[37]

The formation of voids by the Kirkendall effect is well documented and has been previously reported in bulk materials.[25,26] In nanoparticles as well, oxidation is often accompanied by the Kirkendall effect and void formation. In binary alloy NPs, incorporating a noble metal can enhance stability towards oxygen and prevent void formation, as observed in systems such as CuPt.[39] In contrast, binary alloy NPs without this stabilization often exhibit significant void formation during oxidation, as seen in the NiPt system.[35] Various void morphologies have been observed including tetrahedral, octahedral, cubic and hexagonal shapes.[25,40] However, to date, tetrahedral-shaped voids have not been reported in multimetallic NPs. The Kirkendall effect arises from the differential diffusion of Co and Ni during the formation of oxide platelets. This leads to the accumulation of vacancies within the NPs. These vacancies tend to be located at the grain boundaries.[31,41] As previously reported[21] and shown in Fig. 1, CoNiCuPtAu HENAs synthesized *via* PLD are mostly polycrystalline, with only the smallest NPs (under 3 nm) showing monocrystallinity. This structural aspect explains the preferential formation of voids in large NPs. Nevertheless, in very large NPs, we observed the presence of multiple voids. This can be attributed to the low diffusion rate of vacancies, as explained by Railsback *et al.*,[28] which prevents their coalescence into one single void, leading to the stabilization of multiple discrete voids.

It is well established that hollow NPs are thermodynamically unstable. In particular, high-temperature annealing typically drives thermal vacancies toward the outer surface, resulting in the transformation of hollow nanocrystals into solid ones through the shrinkage of the nanovoids.[42] In the present study, contrary to expectations, once voids are formed, they remain remarkably stable and persist at elevated temperatures and during coalescence. This suggests that oxygen plays a key role in stabilizing the [111] facets of the voids. Experimental studies carried out by Landeiro Dos Reis *et al.* revealed that a gaseous atmosphere in fact stabilizes voids and vacancies.[43] Atomic-scale simulations were employed to investigate the stability of nanovoids in FCC NPs interacting with hydrogen, considering various particle shapes and sizes. It was shown that hydrogen atoms, which could infiltrate metal lattices and accumulate near voids, play a critical role in fixing these nanovoids by stabilizing their size, shape, and growth dynamics

compared to hydrogen-free environments. In the present work, the same mechanisms may explain the unexpected stability of the nanovoids observed within CoNiCuPtAu HENAs under an oxygen environment, by stabilizing the inner surfaces either through oxide formation or oxygen adsorption. The formation of oxide surfaces or gas adsorption stabilizes low-energy (111) delimiting crystallographic planes, giving rise to the observed tetrahedral shape.

Our findings can be contextualized by comparison with the gas-cell TEM study of the oxidation of FeCoNiCuPt HENA performed by Song *et al.*[15] Although the study was conducted in air rather than pure oxygen, they still observed the formation of voids due to the oxidation of the transition metals Fe, Co, Cu and Ni. However, the study did not include an analysis of the shape and structure of these voids, only the fact that larger NPs did have multiple voids. In addition, the void size appears to scale with NP diameter: in our case, 5 nm NPs exhibited voids smaller than 1 nm, whereas in the study by Song *et al.*,[15] 50 nm NPs contained voids smaller than 10 nm. Furthermore, as discussed previously, there is an important compositional effect since the substitution of Fe with Au in our NPs prevented the oxidation of Cu, which contrasts with its oxidation observed in FeCoNiCuPt.

In ref. 21, we demonstrated that thermal stability of CoNiCuPtAu HENAs under vacuum is governed by temperature and thermodynamic factors such as surface energy. Under O_2, their thermal stability is influenced not only by temperature, but also by the relative affinity of the five constituent elements towards oxygen. These findings, regarding the differing dominant factors influencing the thermal stability in vacuum and in an O_2 environment are likely to be transferable to other HENAs. However, it is likely that the precise behaviour of the HENAs will depend not only on the elements involved but also on their relative concentrations and interaction. Hence, while the general trends of our observations and comparisons may hold, the specific structural and chemical transformations may vary across HENAs.

5. Conclusions

Despite it being fundamental to real-world gas-related applications, exploration of the behavior of high-entropy nanoalloys in gas environments, particularly under *in situ* or *operando* conditions, remains limited. In this work, we have addressed this gap in quinary HENAs composed of Co, Ni, Cu, Pt and Au. Notably, we employed aberration-corrected environmental scanning transmission electron microscopy combined with energy-dispersive X-ray spectroscopy to directly observe the atomic and compositional evolution of CoNiCuPtAu HENAs under oxygen exposure at atmospheric pressure and elevated temperatures up to 700 °C. This approach allows us to probe their structural and chemical dynamics and interparticle interactions in real time. While particle size distributions appeared stable, *in situ* STEM imaging revealed significant structural dynamics *via* interparticle mass transfer involving particle coalescence and Ostwald ripening. These processes were accompanied by oxygen-induced demixing, leading to the formation of platelet-like Co–Ni oxide structures. These structures were shown to grow epitaxially on the remaining Au-, Pt-, and Cu-rich ternary NPs. Additionally, we observed, for the first time, void formation within larger NPs, attributed to the Kirkendall effect. This study provides direct atomic-scale evidence of the gas-

phase reactivity and structural evolution of CoNiCuPtAu HENAs under oxygen exposure. Contrary to general assumptions of the stability of HEAs, *in situ* environmental STEM observations reveal here that CoNiCuPtAu HENAs undergo pronounced phase segregation and elemental redistribution. It particularly involves the oxidation of less noble components like Co and Ni. Combined with previous knowledge on the thermal stability of CoNiCuPtAu HENAs in vacuum, these findings demonstrate that the thermal stability of HENAs is highly environment-dependent. For tailoring their composition towards more robust catalytic or functional performance under gas environments and at high temperatures, it is thus important that their structure is evaluated under realistic reaction conditions.

Data availability

The data supporting this article have been included as part of the main article and the ESI.†

Conflicts of interest

There are no conflicts to declare.

Acknowledgements

We acknowledge the French National Research Agency for funding the YOSEMITE (ANR-22-CE08-0033) and ARTEMIA (ANR-21-CE42-0012) project and the Region Ile-de-France (convention SESAME E1845) for the double-corrected JEOL ARM 200F electron microscope installed at the Université Paris Cité. This study was supported by the IdEx Université Paris Cité (ANR-18-IDEX-0001). We also acknowledge the doctoral school "EDPIF" for funding the salary of Syrine Krouna.

References

1 Y. Yao, Z. Huang, P. Xie, S. D. Lacey, R. J. Jacob, H. Xie, F. Chen, A. Nie, T. Pu, M. Rehwoldt, D. Yu, M. R. Zachariah, C. Wang, R. Shahbazian-Yassar, J. Li and L. Hu, Carbothermal shock synthesis of high-entropy-alloy nanoparticles, *Science*, 2018, **359**, 1489–1494.
2 X. Wang, W. Guo and Y. Fu, *J. Mater. Chem. A*, 2021, **9**, 663–701, DOI: **10.1039/d0ta09601f**.
3 L. Yang, R. He, J. Chai, X. Qi, Q. Xue, X. Bi, J. Yu, Z. Sun, L. Xia, K. Wang, N. Kapuria, J. Li, A. Ostovari Moghaddam and A. Cabot, *Adv. Mater.*, 2024, **2412337**, 1–53.
4 X. Sun and Y. Sun, *Chem. Soc. Rev.*, 2024, **53**, 4400–4433.
5 W. Al Zoubi, R. A. K. Putri, M. R. Abukhadra and Y. G. Ko, *Nano Energy*, 2023, **110**, 108362.
6 S. K. Dewangan, A. Mangish, S. Kumar, A. Sharma, B. Ahn and V. Kumar, *Eng. Sci. Technol. Int. J.*, 2022, **35**, 101211.
7 Y. Sun and S. Dai, High-entropy materials for catalysis: A new frontier, *Sci. Adv.*, 2021, **7**, eabg1600.

8 L. Yu, K. Zeng, C. Li, X. Lin, H. Liu, W. Shi, H.-J. J. Qiu, Y. Yuan and Y. Yao, *Carbon Energy*, 2022, **4**, 731–761.
9 Y. Xin, S. Li, Y. Qian, W. Zhu, H. Yuan, P. Jiang, R. Guo and L. Wang, *ACS Catal.*, 2020, **10**, 11280–11306.
10 S. Shafeie, S. Guo, Q. Hu, H. Fahlquist, P. Erhart and A. Palmqvist, *J. Appl. Phys.*, 2015, **118**, 184905, DOI: **10.1063/1.4935489**.
11 S. Kumar and M. Kumar, *Trans. Indian Natl. Acad. Eng.*, 2024, **9**, 679–687.
12 F. Marques, M. Balcerzak, F. Winkelmann, G. Zepon and M. Felderhoff, *Energy Environ. Sci.*, 2021, **14**, 5191–5227.
13 H. Xu, J. Zang, Y. Yuan, Y. Zhou, P. Tian and Y. Wang, *J. Alloys Compd.*, 2019, **811**, 152082.
14 X. Yan, W. Yang, Y. Meng, Z. Liao, S. Pang, Q. Wang, P. K. Liaw and T. Zhang, *J. Alloys Compd.*, 2023, **960**, 170757.
15 B. Song, Y. Yang, M. Rabbani, T. T. Yang, K. He, X. Hu, Y. Yuan, P. Ghildiyal, V. P. Dravid, M. R. Zachariah, W. A. Saidi, Y. Liu and R. Shahbazian-Yassar, *ACS Nano*, 2020, **14**, 15131–15143.
16 B. Song, Y. Yang, T. T. Yang, K. He, X. Hu, Y. Yuan, V. P. Dravid, M. R. Zachariah, W. A. Saidi, Y. Liu and R. Shahbazian-Yassar, *Nano Lett.*, 2021, **21**, 1742–1748.
17 Y. Li, C. K. Peng, Y. Sun, L. D. N. Sui, Y. C. Chang, S. Y. Chen, Y. Zhou, Y. G. Lin and J. M. Lee, *Nat. Commun.*, 2024, **15**(1), 1–13.
18 D. Alloyeau, T. Oikawa, J. Nelayah, G. Wang and C. Ricolleau, *Appl. Phys. Lett.*, 2012, **101**, 121920, DOI: **10.1063/1.4754111**.
19 A. Barbero, C. Moreira Da Silva, N. Ortiz Pena, N. Kefane, A. Jaafar, M. Thorey, H. Bouaia, J. Nelayah, G. Wang, H. Amara, C. Ricolleau, V. Huc and D. Alloyeau, *Faraday Discuss.*, 2022, **375**, 129–143.
20 C. Ricolleau, J. Nelayah, T. Oikawa, Y. Kohno, N. Braidy, G. Wang, F. Hue, L. Florea, V. Pierron and D. Alloyeau, *Probe Microsc.*, 2013, **62**(2), 283–293.
21 S. Krouna, A. Acheche, G. Wang, N. O. Pena, R. Gatti, C. Ricolleau, H. Amara, J. Nelayah and D. Alloyeau, *Adv. Mater.*, 2024, **2414510**, 1–10.
22 G. Prévot, N. T. Nguyen, D. Alloyeau, C. Ricolleau and J. Nelayah, *ACS Nano*, 2016, **10**, 4127–4133.
23 D. Alloyeau, G. Prévot, Y. Le Bouar, T. Oikawa, C. Langlois, A. Loiseau and C. Ricolleau, *Phys. Rev. Lett.*, 2010, **105**, 255901, DOI: **10.1103/PhysRevLett.105.255901**.
24 S. Kuboon and Y. H. Hu, *Ind. Eng. Chem. Res.*, 2011, **50**, 2015–2020.
25 A. Meldrum, S. Honda, C. W. White, R. A. Zuhr and L. A. Boatner, *J. Mater. Res.*, 2001, **16**, 2670–2679.
26 Y. Yin, R. M. Rioux, C. K. Erdonmez, S. Hughes, G. A. Somorjal and A. P. Alivisatos, *Science*, 2004, **304**, 711–714.
27 M. Varón, I. Ojea-Jimenez, J. Arbiol, L. Balcells, B. Martínez and V. F. Puntes, *Nanoscale*, 2013, **5**, 2429–2436.
28 J. G. Railsback, A. C. Johnston-Peck, J. Wang and J. B. Tracy, *ACS Nano*, 2010, **4**, 1913–1920.
29 K. Y. Niu, J. Park, H. Zheng and A. P. Alivisatos, *Nano Lett.*, 2013, **13**, 5715–5719.
30 W. Wu and M. M. Maye, *Small*, 2014, **10**, 271–276.
31 J. Huang, Y. Yan, X. Li, X. Qiao, X. Wu, J. Li, R. Shen, D. Yang and H. Zhang, *Nano Res.*, 2020, **13**, 2641–2649.

32 C. M. Wang, A. Genc, H. Cheng, L. Pullan, D. R. Baer and S. M. Bruemmer, *Sci. Rep.*, 2015, **4**, 1–6.
33 W. Xia, Y. Yang, Q. Meng, Z. Deng, M. Gong, J. Wang, D. Wang, Y. Zhu, L. Sun, F. Xu, J. Li and H. L. Xin, *ACS Nano*, 2018, **12**, 7866–7874.
34 L. Han, Q. Meng, D. Wang, Y. Zhu, J. Wang, X. Du, E. A. Stach and H. L. Xin, *Nat. Commun.*, 2016, **7**, 1–9.
35 S. F. Tan, S. W. Chee, Z. Baraissov, H. Jin, T. L. Tan and U. Mirsaidov, *Adv. Funct. Mater.*, 2019, **29**, 1–10.
36 A. Moncomble, D. Alloyeau, M. Moreaud, A. Khelfa, G. Wang, N. Ortiz-Peña, H. Amara, R. Gatti, R. Moreau, C. Ricolleau and J. Nelayah, *Ultramicroscopy*, 2025, **271**, 114121.
37 X. Liu, J. Ruiz and D. Astruc, *Chem. Commun.*, 2017, **53**, 11134–11137.
38 A. Wilson, R. Bernard, Y. Borensztein, B. Croset, H. Cruguel, A. Vlad, A. Coati, Y. Garreau and G. Prévot, *J. Phys. Chem. Lett.*, 2015, **6**, 2050–2055.
39 A. C. Foucher, S. Yang, D. J. Rosen, R. Huang, J. B. Pyo, O. Kwon, C. J. Owen, D. F. Sanchez, I. I. Sadykov, D. Grolimund, B. Kozinsky, A. I. Frenkel, R. J. Gorte, C. B. Murray and E. A. Stach, *J. Am. Chem. Soc.*, 2023, **145**, 5410–5421.
40 S. Kondo, Y. Katoh and L. L. Snead, *Appl. Phys. Lett.*, 2008, **93**, 163110, DOI: **10.1063/1.3005650**.
41 A. A. El Mel, M. Buffière, P. Y. Tessier, S. Konstantinidis, W. Xu, K. Du, I. Wathuthanthri, C. H. Choi, C. Bittencourt and R. Snyders, *Small*, 2013, **9**, 2838–2843.
42 L. Dubau, J. Nelayah, S. Moldovan, O. Ersen, P. Bordet, J. Drnec, T. Asset, R. Chattot and F. Maillard, *ACS Catal.*, 2016, **6**, 4673–4684.
43 M. Landeiro Dos Reis, Y. Ferro, A. Oudriss and X. Feaugas, *Acta Mater.*, 2024, **281**, 120400.